International Journal of Innovative Computing, Information and Control
Volume **21**, Number **3**, June **2025**

ICIC International ©2025 ISSN 1349-4198
pp. **847–858**

NONLINEAR MAGNETICS MODELING FOR DUAL ACTIVE BRIDGE BASED ON HYSTERESIS LOOP PARAMETERS EXTRACTION

Shunshun Ma*, Lexing Zhang and Long Jin

School of Electrical Engineering
Southeast University
No. 2, Sipailou, Xuanwu District, Nanjing 210096, P. R. China
{ 220243163; jinlong }@seu.edu.cn
*Corresponding author: 220225954@seu.edu.cn

Received September 2024; revised December 2024

Abstract. *Dual Active Bridge (DAB) converters are essential in various applications, including DC microgrids, where the nonlinear characteristics of high-frequency transformers interact intricately with other components of the converter. To enhance modeling and simulation accuracy, these nonlinear traits are integrated into the simulations. This paper introduces a novel method that, through Optical Character Recognition (OCR), directly extracts key parameters for the Preisach model from hysteresis loop images, making it widely applicable to different core materials. The accuracy and effectiveness of the model are validated through experimental results from a DAB prototype. Ultimately, this model eliminates the reliance on traditional core test data and can be seamlessly integrated into circuit models to accurately forecast operational waveforms in critical saturation areas.*

Keywords: DAB model, Nonlinear characteristics, Preisach model, Hysteresis loop

1. **Introduction.** Dual Active Bridge (DAB) DC-DC converters play a critical role in DC microgrids due to their low power consumption and soft switching capabilities without the need for additional circuitry [1,2]. Therefore, developing an accurate model of the DAB converter is essential for analyzing its performance. However, a significant challenge in simulation is incorporating the nonlinear characteristics of the actual high-frequency transformer core into the circuit model. This requires electromagnetic modeling of ferromagnetic materials using the permeance-capacitance analogy to replicate the core's static hysteresis behavior. Current research on the Preisach model primarily focuses on the identification of the Preisach function [3-5], with various distribution functions developed for different materials to enhance model accuracy. For example, the Lorentz function is commonly used to approximate the Preisach distribution for silicon steel, while the logistic function is preferred for ferrite materials [6-8]. However, this process can often be cumbersome.

This paper proposes a more versatile method applicable to a wide range of materials. It involves directly fitting the measured limiting hysteresis loop and predicting the hysteresis loop using a transformation formula, thereby simplifying the model development process. If the original data is unavailable and only the image remains, traditional methods typically require re-experimentation to retrieve the data or manual extraction from the image, leading to increased workload and reduced experimental efficiency.

In recent years, Optical Character Recognition (OCR) technology has made significant advancements driven by deep learning and artificial intelligence [9,10]. The primary goal

DOI: 10.24507/ijicic.21.03.847

of OCR is to convert text from images into an editable and searchable format. This paper demonstrates the capability to automatically extract feature data from hysteresis loop images using OCR technology and fit the data with a specific integral function, thereby providing the essential parameters for the development of the Preisach model. The practicality of this approach is confirmed through experimental validation on a DAB platform. Notably, this is the first application of OCR technology in this field, enhancing the innovation and rationale of the research.

The text theme content is divided into four main parts: first, it introduces the specific principles for extracting hysteresis loop parameters based on OCR image recognition technology; second, it describes the construction process of the universal Preisach model and the magnetic equivalent circuit; the third part is experimental validation, comparing the new converter model with the coupled inductance model; finally, it concludes. The entire process is illustrated in Figure 1, from measuring the hysteresis loop in the experimental core to extracting parameters, simulating the magnetic core structure, and finally integrating it into the DAB circuit topology.

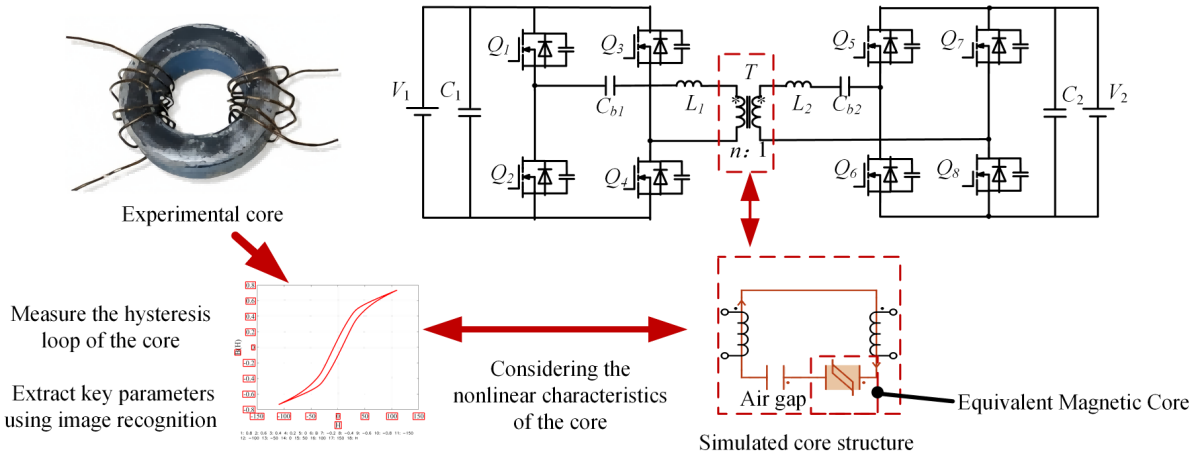

FIGURE 1. Magnetic equivalent simulation circuit structure of DAB converter

2. **Hysteresis Loop Parameter Extraction.** The basic approach involves algorithmically locating the positions of coordinate scales in the image, followed by content recognition. Subsequently, the targeted image undergoes binarization to index pixel content based on the recognized scales, extracting the necessary data. Finally, fitting with appropriate functions yields the corresponding analytical expressions, enabling the arbitrary extraction of desired key parameters.

2.1. **Image feature recognition.** In this study, no existing system was found capable of directly extracting and interpreting axis data from images [11]. To address this, we propose a new method that utilizes Convolutional Recurrent Neural Network (CRNN) and Differentiable Binarization (DB) algorithms to automatically and precisely identify and parse axis scales within images. CRNN combines the feature extraction capability of convolutional neural networks with the sequence modeling ability of recurrent neural networks, making it suitable for handling text sequences within images. Meanwhile, the DB algorithm, through its differentiable binarization approach, can adaptively adjust thresholds and retain more detailed information, thereby enhancing recognition accuracy [12-14].

This method utilizes an advanced Optical Character Recognition (OCR) tool in two main stages: text detection and text recognition. First, the DB algorithm from deep

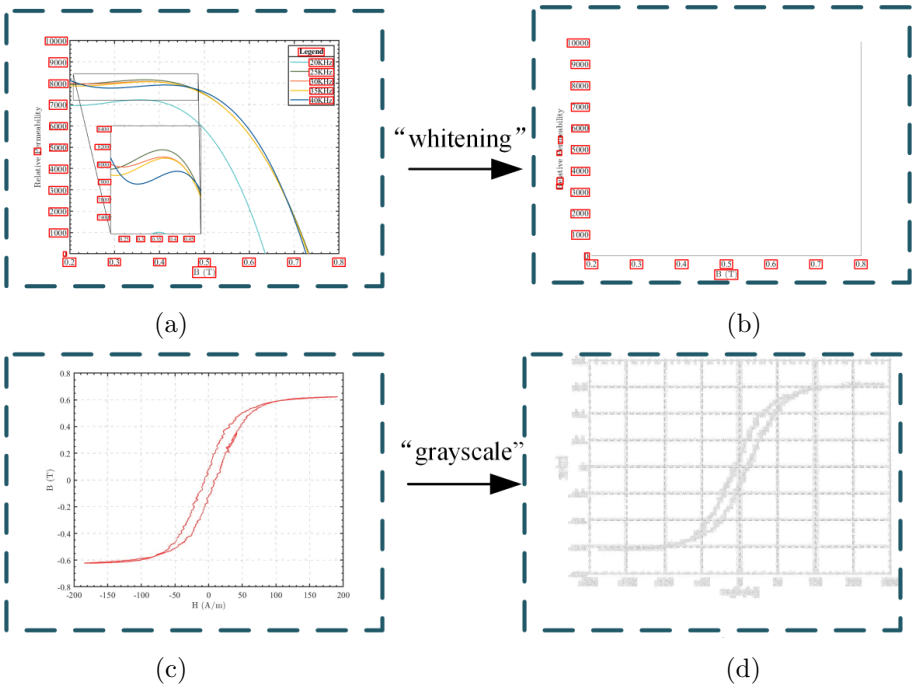

FIGURE 2. Schematic diagram of the result after algorithm processing

learning is used for text detection, identifying text areas and generating bounding boxes, as shown in Figure 2(a). Next, the CRNN algorithm [15] recognizes the text within these boxes. To address the interference caused by irrelevant data detected along the axis, a "whitening" operation is proposed. The main principle involves pixelating the acquired image and summing and comparing the pixels in each row and column. The maximum value within a specified range is identified as the image's boundary. All pixels within this boundary are then set to 255 (white), ensuring that subsequent text localization is not affected by the data within the frame. This approach effectively isolates the relevant areas of the image, allowing for more accurate text detection and recognition. By removing or neutralizing unwanted information, the algorithm can focus on the critical features necessary for processing the text, thereby improving the overall performance of the image recognition system.

$$X_{index} = \max_{i=\text{init}}^{\text{end}} \left(\sum_{j=\text{init}}^{\text{end}} x_{ij} \right) \tag{1}$$

$$Y_{index} = \max_{j=\text{init}}^{\text{end}} \left(\sum_{i=\text{init}}^{\text{end}} x_{ij} \right) \tag{2}$$

After performing the "whitening" operation, the resulting image, as shown in Figure 2(b), is primarily focused on identifying the coordinate axis. To demonstrate the data extraction process, we use the hysteresis loop image depicted in Figure 2(c). Once the image is loaded, grayscale processing [16] is applied to transforming it into pixel blocks with grayscale values ranging from 0 to 255. Each pixel value is represented by X_{ij}, where i denotes the horizontal coordinate and j denotes the vertical coordinate. The variables $X_{\min}$ and $X_{\max}$ define the bottom and top boundaries, while $Y_{\min}$ and $Y_{\max}$ specify the left and right boundaries. The height and width of the image are denoted as H and L, respectively. By observing that the sum of pixel values along the rows and columns at the image's edges is the highest, the image is then split into two sections, each with a

height of $\frac{1}{2}H$ and a width of $\frac{1}{2}L$. The positions of the four boundary coordinates are then determined using Equations (1) and (2).

After extracting the data from the text boxes in Figure 2(b), non-character elements are filtered out using regular expressions. Based on the differences between horizontal and vertical coordinates, the scale sets for the horizontal and vertical axes are determined. Here, $\max_x$ and $\min_x$ correspond to the maximum and minimum values of the horizontal axis scale, while $\max_y$ and $\min_y$ denote the maximum and minimum values of the vertical axis scale. To prevent interference from the grid recognized in Figure 2(d) during further data extraction, pixels with grayscale values near the gray scale are removed. The next step involves traversing the region defined by $[X_{\min} + a, X_{\max} - a]$ and $[Y_{\min} + a, Y_{\max} - a]$ from left to right and from right to left. Here, a is a small value ranging from 3 to 10, used to avoid pixel points that may appear due to the thickness of the border during the data extraction process. The first value encountered that is greater than 0 during this traversal is recorded in the datasets `upper_surface` and `lower_surface`. $H_{(i)\text{lower}}$ is defined as the numerical value of the horizontal coordinate for each point in the `lower_surface` dataset, where i represents the index of the horizontal coordinate position, as shown below:

$$H_{(i)\text{lower}} = (i - X_{\max}) \times \left(\frac{\max_x - \min_x}{X_{\max} - X_{\min}} \right) + \min_x \tag{3}$$

Define $B_{(i)\text{lower}}$ as the vertical coordinate value corresponding to each point in the `lower_surface` dataset, where i denotes the index of the horizontal coordinate and j indicates the index of the vertical coordinate, as expressed below:

$$B_{(i)\text{lower}} = -\left(j - Y_{\min}\right) \times \left(\frac{\max_y - \min_y}{Y_{\max} - Y_{\min}} \right) + \max_y \tag{4}$$

$H_{(i)\text{upper}}$ and $B_{(i)\text{upper}}$ are extracted using a similar process as described above, with the primary distinction being the direction of traversal.

2.2. **Magnetization hysteresis curve fitting.** The data representing the upper and lower surfaces of a hysteresis loop have been extracted, characterizing the hysteresis behavior. Traditional fitting approaches, such as empirical formulas and polynomial fitting, can sometimes result in overfitting due to data noise. To more accurately capture the magnetic hysteresis characteristics, the integral of the arctan function is used for fitting:

$$f(x) = \int_0^H \left(F \cdot \arctan(H_1 - x)\alpha + D\right) dx \tag{5}$$

$$RSS(\beta) = \sum_{i=\text{init}}^{\text{end}} \left(y_i - f(x_i; \beta)\right)^2 \tag{6}$$

The parameters F, H_1, α, and D are optimized by minimizing the Residual Sum of Squares (RSS) using the least squares method. In this context, y_i denotes the observed values, while $f(x_i; \beta)$ represents the output of the function $f(x)$ based on the coefficient set β, which corresponds to the four unknown parameters.

2.3. **Fitting the experimental data using the proposed equation.** In this study, a ferrite ring core made of N87 material was selected, with a magnetic flux path length of 60.179 mm and a cross-sectional area of 48.9264 mm^2. The turns ratio of the transformer is 5 : 5. The experimental setup is shown in Figure 3(a), which includes a 300 μF capacitor for frequency matching. The temperature of the experimental core is controlled using a temperature chamber. In a controlled temperature environment, a sine voltage is applied to the primary winding of the transformer using a signal generator and power amplifier. An oscilloscope captures the primary current and secondary voltage for the magnetization

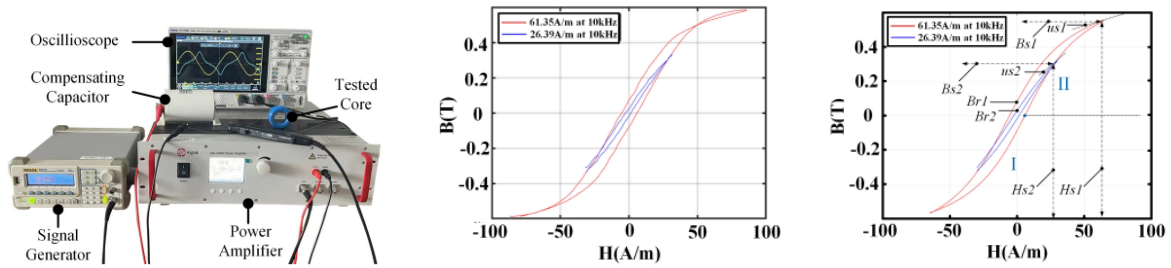

(a) Experimental measurement environment

(b) Experimentally measured curves

(c) The curve obtained by fitting

FIGURE 3. The process of fitting experimental measurements

curve (BH curve) analysis. At 10 kHz, the hysteresis loop was recorded at magnetic field strengths of 61.35 A/m and 26.39 A/m, yielding the data shown in Figure 3(b). To address experimental uncertainties, particularly regarding the measurement accuracy of the oscilloscope and signal generator, regular calibration was performed, and baseline measurements were conducted before each experiment to ensure data accuracy. Using Equation (5), the data were fitted by the least squares method, resulting in Figure 3(c), which extracted the unknowns from Equation (5), thereby fully analyzing the upper and lower branches of the hysteresis loop, making it extremely simple to extract key parameters such as permeability.

3. **Magnetic Equivalent Circuit Model.** From the fitted function, we can readily extract the parameters as illustrated in Figure 3(b). The parameters B_{r1} and B_{r2} represent the remanences of the two hysteresis loops, while B_{s1} and B_{s2} denote the magnetic induction intensities at their respective saturation points. Additionally, μ_{s1} and μ_{s2} are the magnetic permeabilities at these saturation points. The magnetic equivalent circuit model utilizes the permeance-capacitance analogy, which itself is derived from the Preisach model. This model constructs variable magnetic conductance to simulate the static hysteresis characteristics of the iron core. Therefore, the extracted parameters are crucial for analyzing the Preisach model.

3.1. **Preisach model based on logical functions.** The output of the classical Preisach model can be determined using the distribution function $P(U, V)$. To better align with the experimental material requirements, logical functions are employed here as the distribution function:

$$P_s = K \cdot \frac{e^{-(H-H_0)\sigma}}{(1+e^{-(H-H_0)\sigma})^2} \tag{7}$$

Based on this function, the article presents a comprehensive analytical expression for the Preisach model, which facilitates the development of subsequent models:

$$\begin{aligned} B_{irr}^{i} = &-\frac{2K^2}{\sigma^2}\left(\frac{1}{1+e^{-(H_s-H_0)\sigma}}\right)\left(\frac{1}{1+e^{-(H-H_0)\sigma}}-\frac{1}{1+e^{-(H_s-H_0)\sigma}}\right) \\ &+\frac{K^2}{\sigma^2}\left(\left(\frac{1}{1+e^{-(H-H_0)\sigma}}\right)^2-\left(\frac{1}{1+e^{-(H_s-H_0)\sigma}}\right)^2\right)-B_s \end{aligned} \tag{8}$$

B_{irr}^{i} represents the irreversibility component of the increasing branch representation. To offer more flexibility, the arctan integral is utilized to model the reversible component:

$$B_{rev} = \int_0^H (F \cdot \arctan(H_1 - x)\alpha + D)\, dx \tag{9}$$

The unknown parameters such as σ, K, and F, in Equations (8) and (9) are replaced with B_{r1}, B_{r2}, etc., which were determined through graphical methods in the text, to obtain solutions via analytical approaches.

3.2. **Directly fitted Preisach model.** Different distribution functions apply to various materials with varying effectiveness, typically requiring at least two sets of hysteresis loop data. This adds complexity to the experimental process, as extracting parameters from two sets of data leads to a greater number of parameters needed for subsequent magnetic equivalent model establishment. To simplify the experimental procedure, a targeted method is proposed here that allows for direct modeling using only a single set of limiting hysteresis loop data in the Preisach model.

$$B_u^*(H) = 2 \times \mathrm{Intg}(S_6) - \mathrm{Intg}(S_1) \tag{10}$$

$$\mathrm{Intg}(S_1) = 0.5 \times (F(-H_s) - F(H_s))^2 \tag{11}$$

$$\mathrm{Intg}(S_6) = 0.5 \times (f(H_s) + f(-H)) + F(H_s) \times F(-H) \tag{12}$$

$$F(H) = \frac{1}{\sqrt{2}} \times \sqrt{f(-H) - f(H) + \sqrt{2 \times (-f(-H))^2 + 2 \times f(H)^2}} \tag{13}$$

$B_u^*(H)$ represents the expression for the rising branch at a specific H_s (where H_s signifies the maximum magnetic field strength). The function $f(H)$ refers to the fitting equation derived from the material's limiting hysteresis loop. $\mathrm{Intg}(S^*)$ designates the integration region for the Preisach model's variation process, as illustrated in Figure 4.

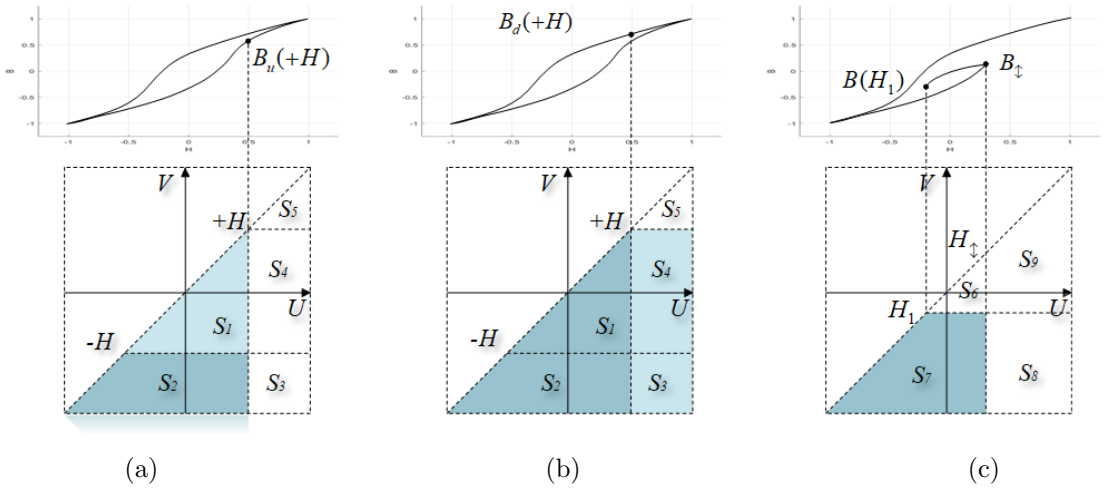

(a) (b) (c)

FIGURE 4. Everett integrals: (a) Limit loop ascending branch; (b) limit loop descending branch; (c) small loop descending branch

3.3. **Construction of magnetic equivalent model in simulation software.** Using image recognition, all parameters necessary for the Preisach model have been successfully fitted. A magnetic core segment module is created in PLECS and integrated into an external circuit. A comparative circuit is also designed to evaluate the differences between the constructed magnetic equivalent model and the actual hysteresis curve.

As shown in Figure 5, the variable permeability is controlled by the differential permeability of the reversible and irreversible components [17,18], using the permeance-capacitance analogy [19] in the magnetic circuit for voltage-current conversion between

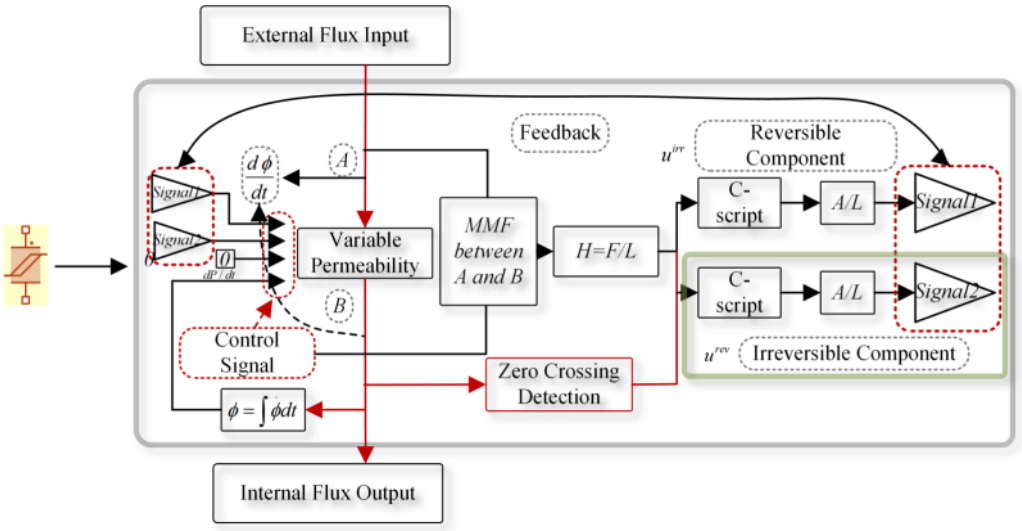

FIGURE 5. The internal structure of the core module

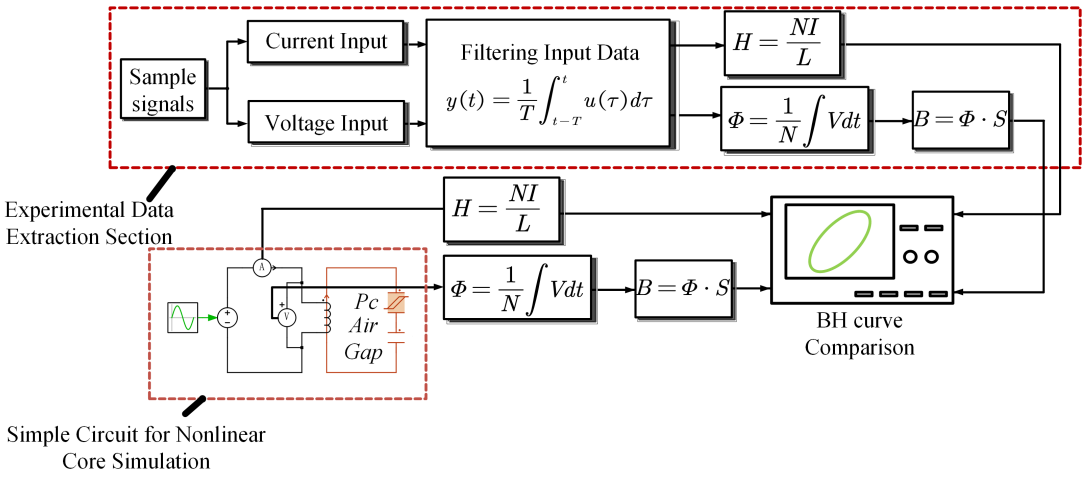

FIGURE 6. Simulation experiments compare and verify the circuit

external circuits. In this context, MMF represents magnetomotive force, Φ represents magnetic flux, μ^{irr} denotes the differential permeability of the irreversible component, and μ^{rev} denotes the differential permeability of the reversible component. In the right part, A and L represent the circumference and cross-sectional area of the measured ring magnetic core, respectively.

Then, the module is applied in software to a simple circuit, like the one in Figure 6, to compare the model's predicted hysteresis return lines with actual data.

The oscilloscope recorded both the primary current and secondary voltage for the BH curve measurements. To validate the methodology, data at H_s values of 50.07 A/m and 38.31 A/m were compared with the simulated core results, as depicted in Figure 7.

As indicated by the fitted images, the fitting results are largely accurate. To verify the accuracy of the parameters, the directly fitted Preisach model is applied in the subsequent DAB circuit.

4. **Construction of DAB Experiment Platform and Simulation Platform.** As shown in Figure 9 is the constructed DAB experimental platform. In the experiment, a core made of T38 material with a cross-sectional area of 82.6 mm^2, a flux path length of

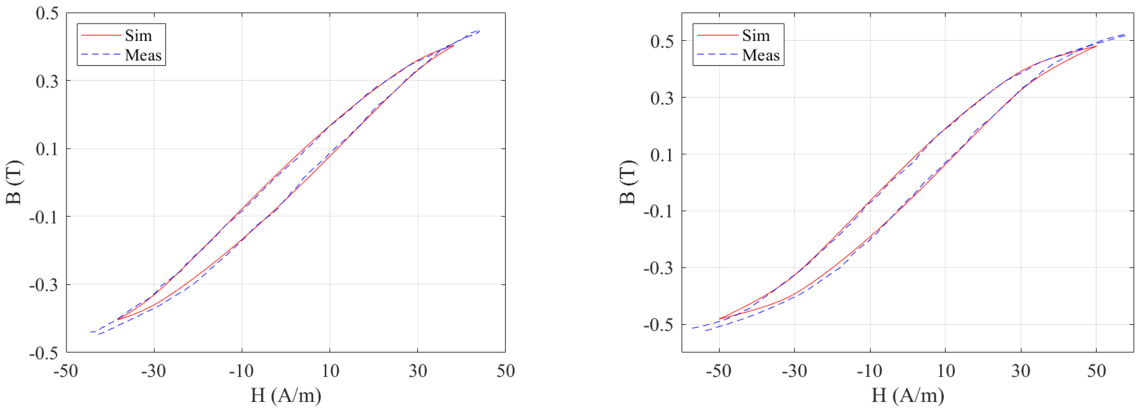

FIGURE 7. Comparison of simulation results with experimental data

171.2 mm, and a primary-to-secondary turns ratio of 5 : 5 was utilized. The excitation signal was a sinusoidal waveform with a peak voltage of $V_p = 18.5$ V at a frequency of 20 kHz. A hysteresis loop with a peak field strength of $H_s = 35.2$ A/m was established as the limiting loop, and the corresponding hysteresis loop was fitted using the previously mentioned method.

4.1. **DAB simulation comparison model setup.** To demonstrate the advantages of this transformer modeling method, it is compared with the traditional coupled inductor model and its three variations of the pure ideal model. Figure 8 shows the traditional coupled inductor model. Given that the transformer used in the experiments has a relatively simple toroidal shape, a high-precision impedance analyzer was employed to perform open-circuit and short-circuit tests on the transformer, allowing the calculation of parameters within the equivalent model [20]. The measured data are presented in Table 1.

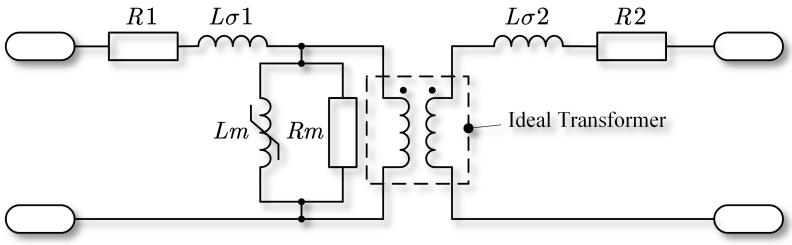

FIGURE 8. Equivalent transformer model of coupled inductance method

TABLE 1. Short-circuit open-circuit test data

Name of experiment	Resistance	Inductance
Secondary open	44.68 Ω	353.01 μH
Secondary short	484.23 mΩ	3.35 μH
Primary open	44.52 Ω	351.88 μH
Primary short	417.47 mΩ	3.27 μH

In the short-circuit experiment, the measured impedances Z_1 and Z_2, and in the open-circuit experiment, the measured impedances Z_3 and Z_4 were obtained for the primary and secondary sides of a completely symmetrical winding transformer. Considering the potential relative error of the instrument, it can be approximated that $Z_1 = Z_2$ and

$Z_3 = Z_4$, indicating that the leakage resistance and leakage impedance of the primary and secondary sides are equal. The calculation process is shown in Equation (14).

$$\begin{cases} R_{\sigma 1} = R_{\sigma 2} = \dfrac{1}{2} \cdot \mathrm{Re}(Z_{\text{short-circuit}}) = 255\ \mathrm{m\Omega} \\ L_{\sigma 1} = L_{\sigma 2} = \dfrac{1}{2} \cdot \mathrm{Im}(Z_{\text{short-circuit}}) = 1.65\ \mu\mathrm{H} \\ R_m = \mathrm{Re}(Z_{\text{open-circuit}}) - R_{\sigma 1} = 22.3\ \Omega \\ L_m = \mathrm{Im}(Z_{\text{open-circuit}}) - L_{\sigma 1} = 176\ \mu\mathrm{H} \end{cases} \tag{14}$$

4.2. **Simulation and experimantal comparative verification of DAB circuits.** The specific parameters of the experimental circuit are listed in Table 2. It is important to note that the series inductor on the experimental platform is an air-core inductor, so its saturation issue does not need to be considered.

Table 2. Simulation and experimental rated parameters

Parameter	Value	Parameter	Value
Input voltage	15 V	Support capacitance 1	100 μF
Output voltage	15 V	Support capacitance 2	100 μF
Switching frequency	20 kHz	Parasitic capacitance	100 pF
Primary series inductance	60 μH	Isolation capacitance	100 μF
Secondary series inductance	50 μH	Transformer turns N	5

In Figure 10, we provide a detailed comparison between the experimental waveforms and the simulated waveforms, with a frequency of 20 kHz and both input and output voltages set at 15 V. Figure 10(a) clearly illustrates the comparison between the experimental and simulated waveforms, where the red line represents the simulated waveform, while the blue line indicates the experimental waveform. It is evident that there is a certain level of consistency in both the shape and amplitude, suggesting that the simulation model accurately reflects the actual scenario. Furthermore, Figures 10(b), 10(c), and 10(d) introduce a comparative analysis of various simulation methods. In these figures, the blue line continues to represent the experimental waveform, the purple line corresponds to the simulation based on the magnetic equivalent circuit, the green line represents the coupled inductor circuit simulation, and the yellow line denotes the results from the pure ideal simulation. Through these comparisons, we can visually observe the differences between the various models, particularly in terms of waveform amplitude and phase characteristics. These comparisons not only help validate the effectiveness of the experimental results but also provide important references for further model optimization.

Figure 10(a) illustrates the secondary bridge arm midpoint voltages V_{H2}, which remain consistent across all three simulation models. The parasitic capacitance in the transformer introduces spike oscillations in the midpoint voltage of the bridge arm during mode transitions, yet the steady-state remains unaffected. Figure 10(b) presents the transformer primary port voltage, Figure 10(c) displays the voltage across the primary series inductor, and Figure 10(d) depicts the current through the secondary series inductor. The partial magnification reveals that the magnetic equivalent circuit offers greater accuracy compared to other models. As the core approaches saturation, the transformer's port voltage and the series inductor voltage exhibit a 'yurt' shaped waveform, while the currents in both the primary and secondary inductors display a 'sharp' waveform. These spike currents, particularly under higher voltage conditions, may pose a risk to the equipment,

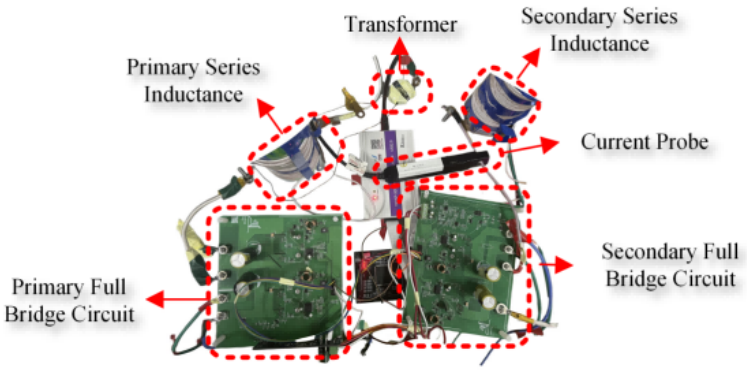

FIGURE 9. DAB experimental platform

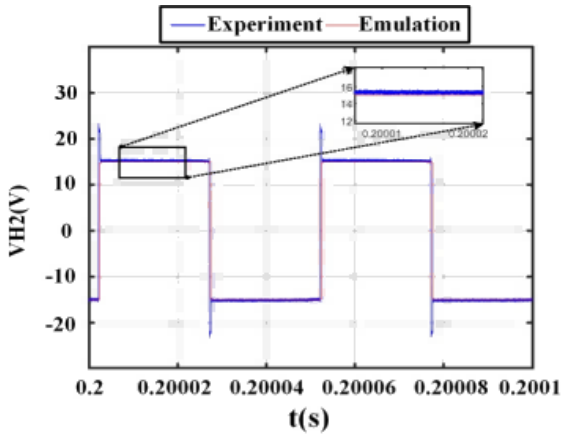

(a) Secondary bridge arm voltage V_{H2}

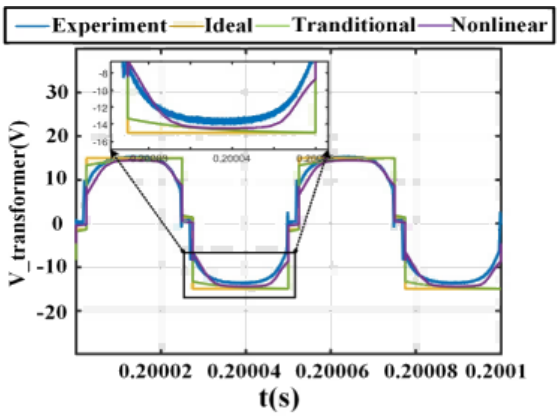

(b) Transformer primary port voltage

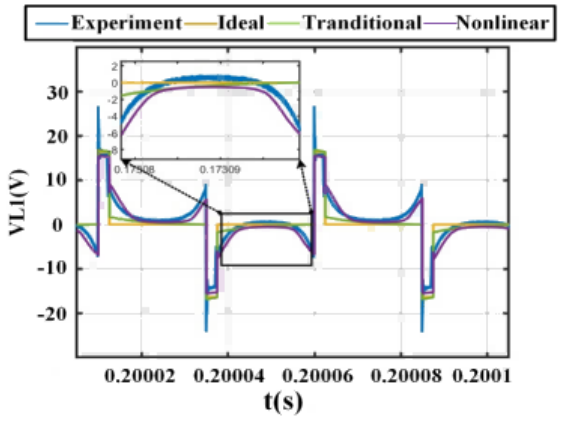

(c) Primary side series inductor voltage

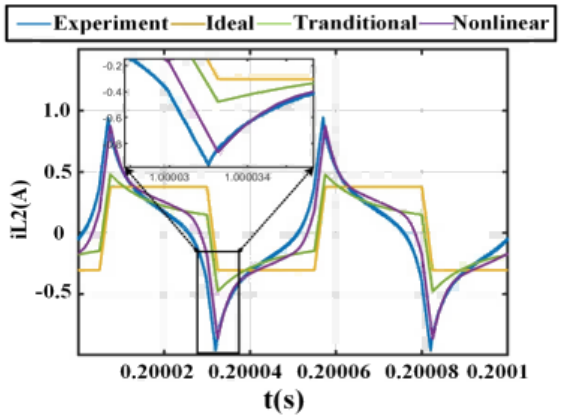

(d) Secondary side series inductor current

FIGURE 10. (color online) Comparison of experimental and simulated waveforms

a situation that can be precisely anticipated by accounting for the nonlinear permeability in the magnetic equivalent circuit.

5. **Conclusions.** This paper presents a new approach for identifying hysteresis loops and extracting critical parameters through the use of Optical Character Recognition (OCR) technology, combined with the Preisach model to enhance the efficiency of electromagnetic circuit simulations. In the case study involving DAB circuit validation, this method

shows improved accuracy over both the conventional coupling inductance model and the idealized model. However, this study also has certain limitations; for example, the proposed method is primarily based on specific experimental conditions and may not be fully applicable to other types of circuit configurations. Additionally, the impact of temperature variations on hysteresis characteristics requires further investigation, which would help better understand the model's applicability under different environmental conditions. Therefore, future research should focus on expanding the application of this method to a broader range of circuit simulations while also exploring its performance under different materials and operating conditions to improve its generalizability and accuracy.

REFERENCES

[1] Y. Ren, Y. Gao, X. Han et al., Frequency-shift hybrid control strategy for backflow power optimization of dual-active-bridge DC/DC converters, *J. Power Supply*, vol.16, no.6, pp.27-33, 2018.

[2] L. Phuc, P. Duc, L. Nhuan et al., Novel resistance control scheme for mitigating current sharing mismatches in parallel dual active bridge converters for DC fast charging stations, *IOP Conference Series: Earth and Environmental Science*, vol.1372, no.1, 2024.

[3] V. De Santis, A. Di Francesco and A. G. D'Aloia, A numerical comparison between Preisach, J-A and D-D-D hysteresis models in computational electromagnetics, *Applied Sciences*, vol.13, no.8, 2023.

[4] Y. Ma, Y. Li, R. Chen, S. Yue and H. Sun, A hybrid dynamic hysteresis model based on the Preisach model and stacked auto-encoder, *International Journal of Applied Electromagnetics and Mechanics*, vol.73, no.4, pp.399-413, 2022.

[5] B. Chen, C. Wang, Y. Liu et al., Dynamic hysteresis modeling method of iron core based on magnetoconductance-capacitance analogy and analytic Preisach model, *J. Electrician Technology*, pp.1-12, 2024.

[6] Y. Li, D. B. Cui and G. Y. Deng, Investigation of the properties of ferrite and graphite modified cement-based materials, *Journal of Materials Science: Materials in Electronics*, vol.35, no.23, DOI: 10.1007/s10854-024-13343-4, 2024.

[7] J. Zhao, W. Zheng, J. Xu and J. M. Zhao, Improved Preisach-DOK modeling on the remanence characteristic of a longitudinal barium ferrite, *International Journal of Digital Content Technology and Its Applications*, vol.7, no.4, pp.258-265, 2013.

[8] M. Luo, D. Dujic and J. Allmeling, Modeling frequency independent hysteresis effects of ferrite core materials using permeance – Capacitance analogy for system-level circuit simulations, *IEEE Transactions on Power Electronics*, vol.33, no.12, pp.10055-10070, 2018.

[9] J. Zhou, C. Yang, Y. Zhu et al., Cross-region feature fusion with geometrical relationship for OCR-based image captioning, *Neurocomputing*, vol.601, 128197, DOI: 10.1016/j.neucom.2024.128197, 2024.

[10] S. Long, X. He, W. Wang et al., PaddleOCR: A high-quality multilingual OCR toolkit, *arXiv Preprint*, arXiv: 2012.11359, 2020.

[11] J. Liu and Z. Deng, Low-light image enhancement using asymmetric convolutional neural networks, *International Journal of Innovative Computing, Information and Control*, vol.20, no.2, pp.479-496, 2024.

[12] X. Li and L. Zhang, Wearable damaged clothing fabric image recognition system based on image restoration algorithm, *Systems and Soft Computing*, vol.620, 200140, 2024.

[13] J. Shen, Container number recognition system based on improved DBNet and improved CRNN, *Industrial Control Computer*, vol.37, no.3, pp.54-56, 2024.

[14] M. Liao, Z. Wan, C. Yao, K. Chen et al., Real-time scene text detection with differentiable binarization, *arXiv Preprint*, arXiv: 1911.08947, 2019.

[15] A. Chowanda, R. Sutoyo, S. Achmad, E. W. Andangsari, S. M. Isa and T.-K. Chen, Modeling emotions recognition on Indonesian product review by combining BERT, CNN, and LSTM architecture, *International Journal of Innovative Computing, Information and Control*, vol.20, no.3, pp.929-944, 2024.

[16] W. Liu, N. Lv, J. Wan et al., Pixel embedding for grayscale medical image classification, *Heliyon*, vol.10, no.16, e36191, 2024.

[17] L. Wang, H. Yao, H. Yang et al., Digital acquisition, processing, and analysis of dynamic hysteresis loops of ferromagnetic materials, *Laboratory Science*, vol.26, no.5, pp.31-35+39, 2023.

[18] B. Chen, F. Wang, N. Wan et al., Analytical Preisach hysteresis model considering reversible component and its characteristic parameter identification algorithm, *High Voltage Technology*, vol.49, no.11, pp.4766-4774, 2023.
[19] Reports from Swiss Federal Institute of Technology Lausanne Highlight Recent Findings in Electronics (Modeling Frequency Independent Hysteresis Effects of Ferrite Core Materials Using Permeance-capacitance Analogy for System-level Circuit ...), *Electronics Newsweekly*, 2019.
[20] Z. Zhao, Y. Zheng, T. Chen et al., High-frequency round wire transformer leakage inductance calculation model based on mirror method, *Proc. of CSEE*, pp.1-12, 2024.

Author Biography

Shunshun Ma received his B.Eng. degree in Electrical Engineering and Automation from Jiangnan University in 2022. He is currently pursuing an M.S. degree in Electronic Information at Southeast University. His research interests include image recognition, modeling of magnetic components, and the application of artificial intelligence in electrical engineering.

Lexing Zhang received the B.Eng. degree in Electrical Engineering from Nanjing University of Astronautics and Aeronautics, Nanjing, China, in 2024. He is currently pursuing the M.S. degree in Electrical Engineering with Southeast University, Nanjing. His research interests include the modeling of magnetic components, and the application of artifical intelligence in electrical engineering.

Long Jin received his master's degree in Automation and Ph.D. degree in Vibration, Concussion, and Noises from the Nanjing University of Aeronautics and Astronautics in 1993 and 1997, respectively. Currently, he is a Professor at the School of Electrical Engineering, Southeast University in Nanjing, China. His research interests cover the design and control of high-power electronics, robotics, and ultrasonic motors.